Void-free buried interface for scalable processing of *p-i-n*-based $FAPbI_3$ perovskite solar modules

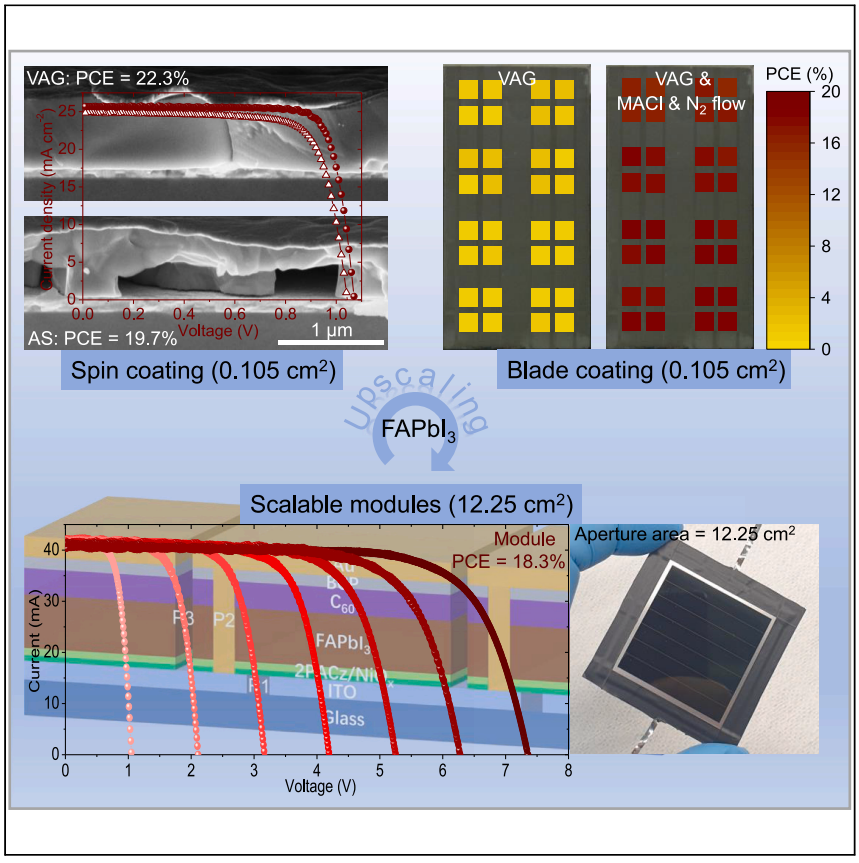

A void-free buried interface in *p-i-n*-based $FAPbI_3$ perovskite solar cells (PSCs) enables to upscale lab-scale solar cells (<1 cm^2) to mini-module dimensions (>10 cm^2). A combined strategy of vacuum-assisted growth, a moderate N_2 flow, and MACl precursor in the crystallization of perovskite layers effectively eliminates interfacial voids as apparent in thin films processed by the anti-solvent method. 22.3% and 18.3% efficiencies are achieved for *p-i-n*-based additive-free $FAPbI_3$ PSCs (0.105 cm^2) and scalable mini-modules (aperture area 12.25 cm^2), respectively.

Void-free buried interface for scalable processing of *p-i-n*-based $FAPbI_3$ perovskite solar modules

Hang Hu,[1,2] David B. Ritzer,[1,2] Alexander Diercks,[2] Yang Li,[1,2] Roja Singh,[1,2] Paul Fassl,[1,2] Qihao Jin,[2] Fabian Schackmar,[1,2] Ulrich W. Paetzold,[1,2,*] and Bahram Abdollahi Nejand[1,2,3,*]

SUMMARY

Formamidinium lead iodide ($FAPbI_3$) has emerged as one of the most promising perovskite semiconductors for perovskite solar cells (PSCs), demonstrating high power conversion efficiency (PCE) and good stability. However, only a few reports address the scalable pro-cessing and fabrication of $FAPbI_3$ perovskite solar modules. Here, we report a void-free perovskite-buried interface in *p-i-n*-based PSCs, which enables us to upscale lab-scale solar cells (<1 cm^2) to mini-module dimensions (>10 cm^2). An innovative combination of a mod-erate N_2 flow during vacuum-assisted growth (VAG) control of the perovskite thin films as well as the employment of MACl as an addi-tive eliminates interfacial voids in blade-coated large-area $FAPbI_3$ layers, enabling respective PCEs of 20.0% and 18.3% in blade-coated PSCs (0.105 cm^2) and fully scalable modules (aperture area of 12.25 cm^2 and geometric fill factor of 96.3%). This is a remarkable advance in upscaling $FAPbI_3$-based perovskite photovoltaics.

INTRODUCTION

Perovskite photovoltaics developed into one of the most promising photovoltaic technologies over the past decade with certified power conversion efficiencies (PCEs) exceeding 25%[1] for lab-scale devices (area <1 cm^2). Among the material class of lead halide perovskite semiconductors, formamidinium lead iodide ($FAPbI_3$) is an efficient and widely used candidate with a rather low band gap (~1.48 eV) close to the optimum of the detailed balance theory (1.1–1.4 eV)[2] and good thermal stability of the black cubic phase (α-$FAPbI_3$).[2–4] To date, the highest PCEs (>23%) of $FAPbI_3$ perovskite solar cells (PSCs) have been reported for the *n-i-p* architecture,[5–11] whereas the *p-i-n* architecture, which is particularly interesting for most state-of-the-art perovskite-based tandem solar cells,[1,12] can be processed at low temperatures[13–15] and offers good operational stability. How-ever, the recently reported record PCEs for *p-i-n*-based $FAPbI_3$ PSCs ~22.13%[16,17] still lag behind significantly in terms of PCE, scalability, and active area compared with the *n-i-p* architecture.

The key challenge in processing pure $FAPbI_3$ thin films is the instability of the photo-active α-$FAPbI_3$ phase, which tends to convert into the photoinactive yellow ortho-rhombic phase (δ-$FAPbI_3$) at room temperature, especially in the presence of mois-ture or polar solvents.[18–20] To overcome this challenge, numerous strategies have been proposed to stabilize α-$FAPbI_3$ and improve crystallization/thin film morphology, including additive engineering (e.g., hydrohalic acid,[21–24] ionic liq-uids,[9] Lewis base,[25,26] 2D species,[27] and others[28–30]); compositional engineering (cations,[31–34] e.g., methylammonium (MA^+), Cs^+, Rb^+; anions, [5,7,10,35] e.g., Br^-,

CONTEXT & SCALE

In recent years, remarkably promising performance was reported for $FAPbI_3$ perovskite solar cells; however, the scalability lags behind. Key challenges regarding the scalable processing of $FAPbI_3$ solar modules are the high-quality large-area perovskite thin film fabrication, interface engineering, and interconnection module patterning. In particular, little research was dedicated so far toward optimizing buried interface in *p-i-n* based $FAPbI_3$ devices.

In this work, a combination of vacuum-assisted growth, N_2 flow, and MACl additive moderates the crystallization of perovskite thin films and realizes void-free buried interface. This strategy allows us to improve photovoltaic performance due to reduced non-radiative recombination and enhanced charge extraction. We realize high-efficiency *p-i-n* based $FAPbI_3$ solar cells and fully scalable modules and thus providing an effective approach and more opportunities for upscaling perovskite photovoltaics.

Cl^-); and interfacial engineering (organic ammonium halides to form 2D perovskites,[5,7,35–38] polymer[39,40]). We highlight that these approaches have been widely developed for *n-i-p*-based PSCs, but only very few studies report on *p-i-n*-based $FAPbI_3$ PSCs, with PCEs in the range of only 20%–22.1%.[16,17,41,42] Among the most promising approaches is interfacial/compositional engineering employing methylammonium chloride (MACl), which was successfully implemented in *p-i-n*-based $FAPbI_3$ PSCs as surface post-treatment[41] and precursor additive[17] to improve the perovskite thin film morphology. The latter also showed that [2-(3,6-Dimethoxy-9H-carbazol-9-yl)ethyl] phosphonic acid (MeO-2PACz) is a superior hole transport layer (HTL) compared with other selected HTLs for stabilizing α-$FAPbI_3$ with passivated defects at grain boundaries, thus decreasing the open-circuit voltage (V_{OC}) loss.[17] We note that in *p-i-n*-based $FAPbI_3$ PSCs, perovskite-buried interface has not been investigated yet. However, this interface is key to photovoltaic performance and device stability.[43–45] For instance, the buried interface in PSCs is known to exhibit uncoordinated Pb^{2+} defects or interfacial voids (e.g., loose interfacial contact), leading to non-radiative recombination or poor charge carrier extraction/transport and consequently a large loss in V_{OC} or short-circuit current density (J_{SC}).[45,46] In stark contrast, numerous studies have reported on improving the electron transport layer (ETL)/perovskite interface in *n-i-p*-based $FAPbI_3$ PSCs. The presence of mesoporous TiO_2 proved to improve the photovoltaic performance due to good charge extraction (CE), and simultaneously, a reduced degradation rate was observed for samples exposed to ambient air.[3,47] The good charge carrier extraction explains the high J_{SC} in many PSCs with an *n-i-p* architecture. Therefore, improving the buried interface in *p-i-n*-based $FAPbI_3$ PSCs is key to improving CE, reducing non-radiative recombination and enhancing the phase stability of PSCs.

Next to improving the PCE and stability of *p-i-n*-based $FAPbI_3$ PSCs, upscaling small-area spin-coated $FAPbI_3$ devices with scalable methods is a key challenge. To date, the scalable fabrication of high-purity $FAPbI_3$ PSCs is barely investigated, apart from two reports on blade-coated *p-i-n*-based $FAPbI_3$ PSCs (PCE = 18.41%, active area of 0.09 cm^2)[48] and perovskite solar mini-modules[42] (reported PCE = 17.07% for an active area of 12.32 cm^2 and PCE = 12.52% for an aperture area of 25 cm^2 and a geometrical fill factor [GFF] of 73.3% according to our calculation). Scalable solution-based fabrication involves solvent engineering and compositional engineering to optimize the perovskite thin film crystallization.[13] Controlling the nucleation and crystallization during scalable process are extremely pivotal to achieve high-quality, pinhole-free, void-free, and homogeneous perovskite thin films that are thoroughly associated with the solvent evaporation process. Prompt extraction of solvents from the wet perovskite precursor thin films is required to process compact and pinhole-free perovskite thin films.[49] Therefore, a good control of the drying process and solvent engineering are pivotal to optimize the thin film morphology and eventually the homogeneity of perovskite thin films.[50] The co-solvent (volatile and non-volatile) system composing acetonitrile, 2-methoxyethanol, or ethyl alcohol mixed with common inks dimethylformamide (DMF)/dimethyl sulfoxide (DMSO) has been widely used to improve the quality of large-area perovskite thin films and buried interface.[49,51] Recently, DMSO was replaced by the Lewis base N-methyl-2-pyrrolidone and hydriodic acid to regulate the intermediary phase in blade-coated $FAPbI_3$ perovskite mini-modules.[42] Furthermore, N_2-knife-assisted drying for blade coating is a promising strategy to control film quality and slow down crystallization.[15,45,51,52] To date, the morphology formation of blade-coated $FAPbI_3$ thin films processed from the inks based on conventional solvent systems of DMF/DMSO and the interplay with the HTL has not been studied.

In this study, we report on the vacuum-assisted growth (VAG) method to process high-quality α-$FAPbI_3$ PSCs in the *p-i-n*-based architecture. The conventional reference process, using an anti-solvent (AS) step, exhibits voids at the buried interface of HTL/$FAPbI_3$. In contrast, our VAG-processed $FAPbI_3$ thin films are free of interfacial voids, leading to a champion PCE of 22.3% for *p-i-n*-based PSCs. Our study shows that the voids lead to high V_{OC} loss associated with increased non-radiative recombination and low J_{SC} due to poor CE. Finally, we report on large-area blade-coated $FAPbI_3$ thin films. To avoid the formation of voids and control the morphology of these $FAPbI_3$ thin films, we incorporate MACl as an additive into the perovskite precursor and further apply a moderate N_2 flow during the VAG process. As a result, we obtain homogeneous large-area blade-coated $FAPbI_3$ thin films on different HTLs that enable blade-coated PSCs (0.105 cm^2) and perovskite solar module (aperture area of 12.25 cm^2, GFF = 96.3%) with a PCE of 20.0% and 18.3%, respectively.

RESULTS AND DISCUSSION

The VAG method is an established strategy to process high-quality narrow and wide band-gap PSCs as well as two-terminal (2T) all-perovskite tandem solar modules.[15,53,54] In this study, we employ VAG method to fabricate $FAPbI_3$ PSCs in the *p-i-n* architecture. First, we report on spin-coated small-area PSCs. The lab-scale PSCs exhibit an active area of 0.105 cm^2 with the layer stack glass/indium tin oxide (ITO)/[2-(9H-carbazol-9-yl)ethyl] phosphonic acid (2PACz)/$FAPbI_3$/fullerene (C_{60})/2,9-dimethyl-4,7-diphenyl-1,10-phenanthroline (BCP)/Au (Figure 1A). The photovoltaic performance of the PSCs fabricated by VAG using different vacuum times (15, 30, 45, 60, and 120 s) is compared with devices processed with the established AS quenching method. For both fabrication methods, the perovskite absorber layers exhibit a similar thickness of ∼700 nm (Figure S1). We find that the PSCs fabricated with VAG (referred to as VAG-PSCs) demonstrate higher yield and better reproducibility compared with the PSCs fabricated by AS (referred to as AS-PSCs) (Figure 1B). The AS-PSCs exhibit an average PCE of 17.2%, whereas VAG-PSCs show an average PCE of around 20.7% for optimized vacuum time (∼30 s). Both shorter and longer vacuum times lead to significantly lower performance. To further improve the performance of these PSCs, we optimize the light incoupling in our champion device using a MgF_2 antireflection coating, resulting in an even higher PCE of up to 22.3% (FF of 0.81, V_{OC} of 1.07 V, and J_{SC} of 25.7 mA cm^{-2}) (Figure 1C). We highlight that—to the best of our knowledge—this is the highest PCE value reported for *p-i-n*-based pure $FAPbI_3$ PSCs without additives and significantly exceeds the reference AS-PSC (PCE of 19.7%, FF of 0.76, V_{OC} of 1.04 V, and J_{SC} of 24.8 mA cm^{-2}). Furthermore, our champion VAG-PSC exhibits a stabilized power output efficiency (SPCE) of up to 21.8% for maximum power point (MPP) tracking for 5 min under continuous AM 1.5G (100 mW cm^{-2}) irradiation (Figure 1D). We attribute the prominent enhancement in V_{OC} for our VAG-PSCs with a band gap of ∼1.52 eV (Figure S2A) to the reduced non-radiative recombination (detailed discussion follows). A broadband enhancement in the external quantum efficiency (EQE) of VAG-30-s PSCs is observed compared with the reference AS-PSCs (Figures 1E and S3), leading to an enhancement in J_{SC} from 24.0 to 24.9 mA cm^{-2}. The latter is not attributed to changes in light harvesting (Figure S2) but is rather a result of improved charge carrier extraction governed by improved buried interface across the ITO/2PACz/$FAPbI_3$ layer stack[45] as discussed in the following.

Next to the device performance, we examine the morphology of the $FAPbI_3$ thin films. First, we note the obvious and large number of "white" spots, whose origin is discussed later. These white spots are apparent in the AS-PSCs by visual inspection

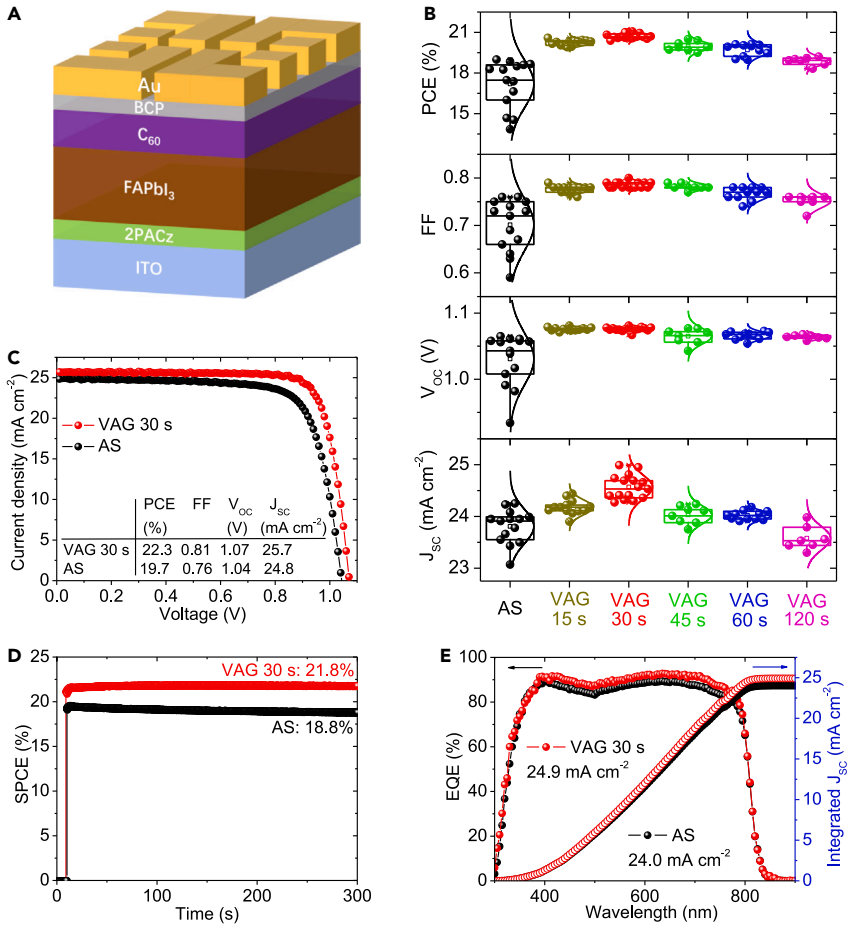

Figure 1. Photovoltaic performance of spin-coated PSCs

(A) Schematic of *p-i-n*-based $FAPbI_3$ PSCs.

(B and C) (B) Statistical distribution of photovoltaic parameters and (C) current density-voltage (*J-V*) characteristics of PSCs fabricated using anti-solvent (AS) quenching and vacuum-assisted growth (VAG). The vacuum time is varied from 15 to 120 s.

(D and E) (D) Stabilized power conversion efficiency (SPCE) under continuous AM 1.5G illumination and (E) external quantum efficiency (EQE) spectra for the best-performing PSCs (with MgF_2 antireflection coating).

from the glass side (Figure 2A). The density of the white spots varies with vacuum time for VAG-PSCs. Interestingly, the white spots almost vanish for a vacuum time of around 30 s, which coincides with the optimum device performance (Figure 1B). Inspection by optical microscopy (from the glass side, Figure 2B) reveals that the samples processed with short VAG times (<30 s) exhibit problematic cracks. These cracks are attributed to an incomplete solvent extraction which triggers the formation of cracks and corresponding voids during the annealing step (Figures 2B and S4). For increasing VAG times (>30 s), the samples exhibit the defects with an increasing number and expanding size that are obviously detrimental to the quality of perovskite thin film. For long vacuum times, these defects span over the entire glass region (i.e., ITO-etched area, in Figure S4), and the spot dimensions increase to several hundreds of micrometers (for VAG times $\geq$60 s). We confirm that these spots are eventually voids at the buried interface of 2PACz/$FAPbI_3$ by cross-sectional scanning electron microscopy (SEM) images (Figures 2C and S4). The appearance of such voids upon imperfect crystallization is a phenomenon that was already reported in literature for other

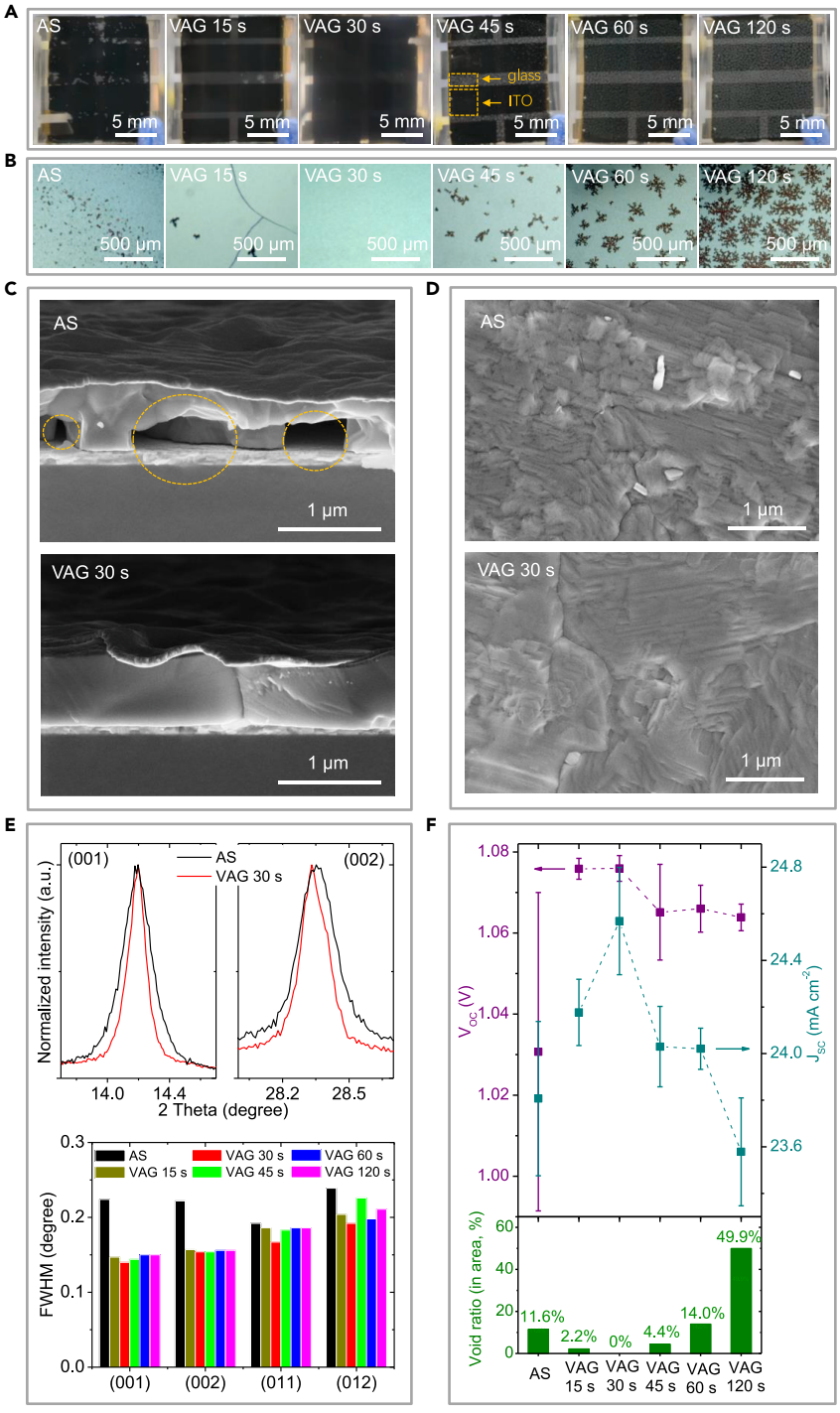

Figure 2. Spin-coated perovskite thin films

(A and B) Photographs (A) and (B) optical microscopic images of *p-i-n*-based $FAPbI_3$ PSCs (glass side, substrate: 1.6 × 1.6 cm^2) fabricated via anti-solvent (AS) quenching and vacuum-assisted growth (VAG) method. The VAG time varies from 15 to 120 s. The white spots in (A) and dark region in (B) indicate voids.

(C and D) (C) Cross-section and (D) top-view scanning electron microscopy (SEM) images.

(E) Zoom-in peaks of X-ray diffraction (XRD) patterns and full width at half maximum (FWHM) for different $FAPbI_3$ thin films.

(F) Relationship between the void ratio, V_{OC}, and J_{SC} of PSCs.

high-efficiency mixed-cation perovskites containing DMSO solvent.[5,7,45,55] The phenomenon is more evident in thick and large-area perovskite films.[45] The appearance of these voids near the 2PACz/$FAPbI_3$ interface is attributed to a volume collapse of the wet perovskite film during the drying and/or crystallization step. This volume collapse occurs if homogeneous and steady solvent extraction is prohibited due to the formation of an impermeable perovskite thin film that is formed at the top of the wet film, leaving behind enclosed voids filled with solvent at the 2PACz/$FAPbI_3$ interface. During the annealing step, the trapped high-boiling-point solvents like DMSO will expand and cause voids and corrupted thin films.[45] These voids are expected to increase with increasing vacuum time (e.g., >30 s). For optimum VAG time (30 s), an equilibrium between the solidification of the perovskite thin film and the extraction of the high boiling solvents (e.g., DMSO) is achieved. As a consequence, a homogeneous and void-free perovskite thin film with comparably large grains is fabricated as shown also in a detailed analysis of the thin film morphology by means of SEM and atomic force microscopy (AFM) (Figures 2D and S5). It is highlighted that the cracks in the range of micrometers are distinguishable at AS and VAG-15-s perovskite thin films (Figure S6). The X-ray diffraction (XRD) patterns (Figure S7A) confirm that the annealed $FAPbI_3$ thin films form the α-phase with the expected diffraction peaks.[6,16] VAG-30-s thin films exhibit a reduction of full width at half maximum (FWHM) for the diffraction peaks, especially in (001) and (002) planes (Figures 2E and S7B), which reflects the larger size of crystallites. An apparent PbI_2 peak (Figure S7A) is observed since 10 mol % of excess PbI_2 is used as a standard recipe for preparing perovskite precursor, which has been proved decreased trap states for *p-i-n*-based $FAPbI_3$ PSCs.[17] Note that the excess PbI_2 in this work assists to obtain void-free $FAPbI_3$ thin films (Figure S8A). The $FAPbI_3$ thin film processed with excess PbI_2 shows no changes in the light harvesting and band gap of perovskite (Figures S8B–S8D) but delivers improved device performance with increased V_{OC}, J_{SC}, and FF (Figure S9).

We hypothesize that the buried voids isolate parts of the perovskite thin film from the HTL and, thereby, impede efficient CE, resulting in reduced current generation (Figure 1B). Moreover, the voltage decreases due to enhanced non-radiative recombination losses caused by the increased trap states at the surface of buried voids, as will be discussed later in this work. We show that the void ratio in the area provides a quantifiable measure that correlates with the impact of the voids on the device performance, i.e., the J_{SC} and the V_{OC} (Figure 2F). For vacuum times $\leq$45 s, we show that the VAG-$FAPbI_3$ thin films exhibit low void ratios <5% compared with a much larger void ratio >11.5% for AS-$FAPbI_3$ thin films. With further increasing vacuum time up to 120 s, the void ratio increases to 49.9% due to a larger size of voids and an increased number of voids (Figure 2B).

The previous findings demonstrate that the VAG method is an efficient route to fabricate high-quality $FAPbI_3$ thin films for high-efficiency *p-i-n*-based PSCs. The improved device performance compared with AS-PSCs is governed by an increase in V_{OC} and J_{SC}. To shed light on the origin of these improvements, we conduct a series of material and photophysical characterization experiments to investigate the non-radiative recombination (related to increased V_{OC}) and CE (associated with increased J_{SC}). First, to understand V_{OC} improvement, we study the charge carrier dynamics for a half stack of the PSC using time-resolved photoluminescence (TRPL). We fabricate $FAPbI_3$ thin films on glass/ITO/AlO_x (as an insulating interlayer) and glass/ITO/2PACz (as an HTL). A thin solution-processed layer of ethylene-vinyl-acetate copolymer is used for protecting the $FAPbI_3$ thin films against moisture while measuring them in the air atmosphere. As shown in Figure 3A, the glass/AlO_x/

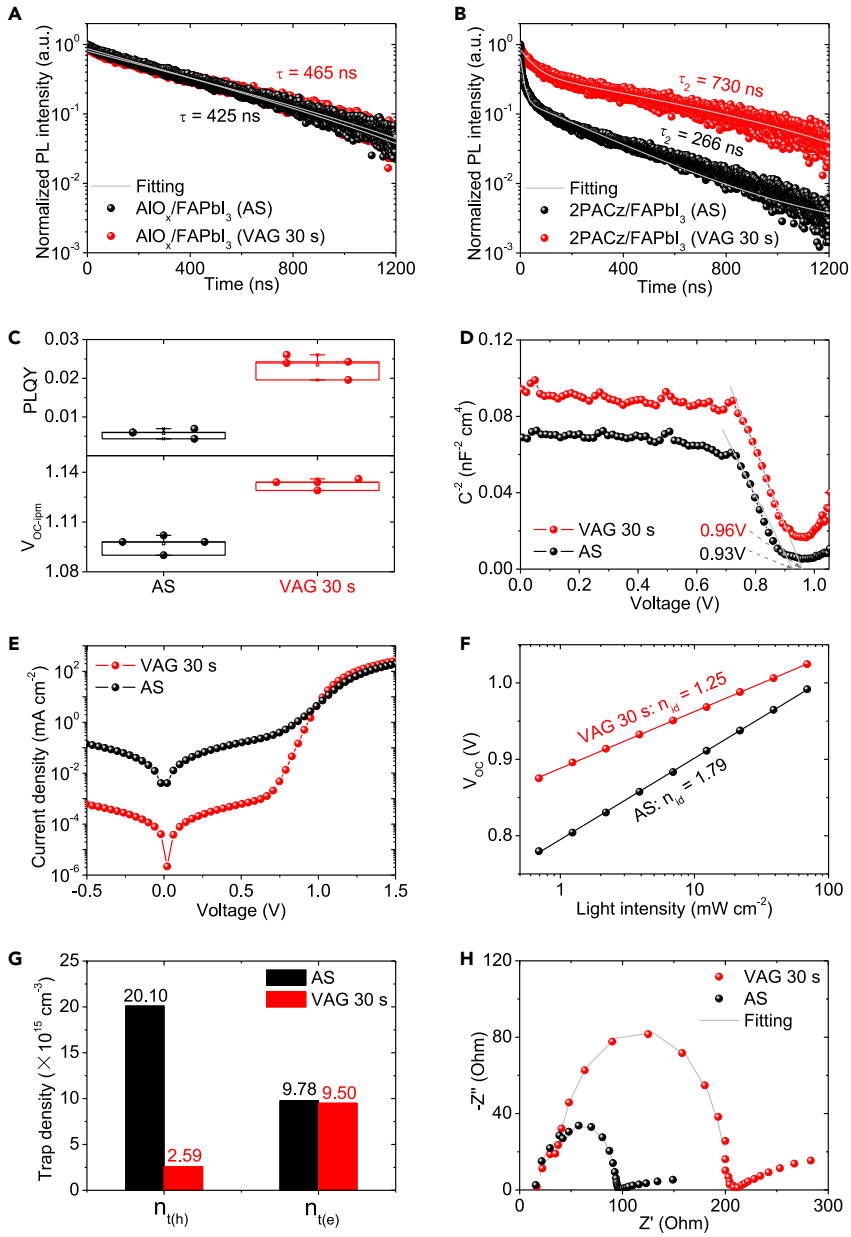

Figure 3. Characteristics of non-radiative recombination

(A and B) Time-resolved photoluminescence (TRPL) of $FAPbI_3$ thin films on (A) ITO/AlO_x (as an insulating layer) and (B) ITO/2PACz substrates.

(C) Photoluminescence quantum yield (PLQY) and the obtained implied V_{OC} ($V_{OC\ imp}$) of $FAPbI_3$ thin films prepared on ITO/2PACz Substrates.

(D–F) (D) Mott-Schottky plots, (E) dark current density-voltage (*J-V*) curves, and (F) light intensity dependence of the V_{OC} of PSCs.

(G) Hole and electron trap density ($n_{t(h)}$ and $n_{t(h)}$) obtained from space-charge-limited current (SCLC) method.

(H) Nyquist plots and (symbols) and fitting curves (solid lines) of PSCs measured in the dark with an applied bias of 1 V (close to V_{OC}).

$FAPbI_3$ layer sequence exhibits a single-exponential decay. The fitted lifetime τ is dominated by non-radiative recombination at grain boundaries and the bulk of $FAPbI_3$ thin films.[5,53,54] Compared with the AS thin film, a slight increase in τ from

425 to 465 ns for the VAG-30-s thin film indicates less trap-assisted non-radiative recombination of the perovskite layer. This difference is attributed to the improved grain size of perovskite with fewer grain boundaries. For comparison, the architecture glass/ITO/2PACz/$FAPbI_3$ exhibits a biexponential decay with a fast and a slow charge carrier lifetime τ_1 and τ_2, respectively (Figure 3B). We attribute τ_1 to the fast charge transfer process from perovskite to 2PACz, whereas τ_2 is associated with the non-radiative recombination at grain boundaries and bulk and/or the buried interface of 2PACz/$FAPbI_3$.[54,56–58] Interestingly, the value of τ_2 for VAG-30-s thin film (730 ns) is much higher than that of AS thin film (266 ns) (see Tables S1). According to the comparison of τ in Figure 3A, the significantly enhanced τ_2 is attributed to the reduced non-radiative recombination at the buried interface of 2PACz/$FAPbI_3$ due to reduced interfacial defects.[59]

We further quantify the reduction of non-radiative recombination for the half-layer stack of ITO/2PACz/$FAPbI_3$ via photoluminescence quantum yield (PLQY) measurements and calculate the corresponding implied V_{OC} ($V_{OC\text{-}imp}$).[59,60] As presented in Figure 3C, the AS sample exhibits an average PLQY of 5.8×10^{-3}, whereas the VAG-30-s sample exhibits a PLQY increase by one order of magnitude to around 2.3×10^{-2}. The corresponding average $V_{OC\text{-}imp}$ increases from 1.097 to 1.133 V that implies significantly reduced non-radiative recombination for the VAG-30-s sample. Since the absolute enhancement matches well with the average increase in V_{OC} observed in the corresponding PSCs (Figure 1B), this further indicates that it is indeed reduced non-radiative recombination at the 2PACz/$FAPbI_3$ interface that causes the increased device V_{OC}, which will be studied in more detail in the following paragraphs.

Next to optical spectroscopy of half-stacks, we examine the reduced non-radiative recombination of full devices. First, Mott-Schottky plots, derived from capacitance measurements (Figure 3D), reveal a higher flat-band potential of 0.96 V for a representative VAG-30-s PSC compared with an AS-PSC that yields 0.93 V. This suggests an enhanced driving force for separating photogenerated charge carriers which is favorable to realize a higher V_{OC}.[61,62] This observation is further confirmed by the dark current density-voltage (*J-V*) characteristics (Figure 3E) and light-intensity-dependent V_{OC} measurement (Figure 3F). We observe that the VAG-30-s PSC shows a significantly reduced dark saturation current density ($J_0 = 4.07 \times 10^{-12}$ mA cm^{-2}) and a lower ideality factor ($n_{id} = 1.25$) compared with AS-PSC ($J_0 = 2.45 \times 10^{-5}$ mA cm^{-2}, $n_{id} = 1.79$), supporting our interpretation of less trap-assisted non-radiative recombination at the interfaces.[54,63]

To investigate the origin of reduced non-radiative recombination, we utilize space-charge-limited current (SCLC) to estimate the trap density (n_t).[5,54,64–67] As discussed above, the interfacial trap states are expected to dominate the trap-assisted non-radiative recombination compared with those in the bulk of perovskite (Figures 3A–3C). The interfacial trap states can originate from the defects at the buried 2PACz/$FAPbI_3$ or top $FAPbI_3/C_{60}$ interfaces. These trap states capture and trap free charge carriers, thereby increasing non-radiative recombination.[5] For SCLC analyses, we fabricate electron- and hole-only devices in the architecture of ITO/SnO_2/$FAPbI_3$/C_{60}/BCP/Au and ITO/2PACz/$FAPbI_3$/Poly(3-hexylthiophen-2,5-diyl) (P3HT)/Au, respectively. The calculation details can be found in the supplemental experimental procedures and Figure S10. Notably, the hole trap density ($n_{t(h)}$) of the VAG-30-s device is calculated to be 2.59×10^{15} cm^{-3} (Figure 3G), which is one order of magnitude lower than that of the AS device (20.10×10^{15} cm^{-3}). As reported in literature, the buried interfaces, especially the interface with the voids, contain numerous uncoordinated Pb^{2+} or FA^{+} vacancy

defects that lead to enhanced non-radiative recombination.[5,45,46] We speculate the high $n_{t(h)}$ in the AS device is due to the emerging of the voids at the buried interface of 2PACz/$FAPbI_3$, whereas the $n_{t(h)}$ reduces significantly in the VAG-30-s device due to the elimination of the interfacial voids (Figures 2A–2C and S4). In addition, we show that the electron trap density ($n_{t(e)}$) of VAG-30-s device is slightly lower compared with AS device. This is attributed to the void-free buried interface of SnO_x/$FAPbI_3$ (for AS and VAG) and improved morphology of electron-only devices (Figure S11A). Commonly, SnO_x has a better interfacial contact with perovskite, and thus, the void-based buried interface is not so common in *n-i-p* architecture. SnO_x is significantly more hydrophilicity compared with 2PCAz monolayers (Figure S11B). Therefore, the interplay between perovskite and SnO_x during the VAG process is different compared with the case of using organic HTLs beneath. This may further affect perovskite formation and crystallization.[46] Since $FAPbI_3$ thin films fabricated via VAG do not show notable changes in surface morphology (i.e., forming $FAPbI_3$/C_{60} interface) compared with the AS quenching method (Figures 2D and S5), we conclude that the enhanced non-radiative recombination loss in AS-PSCs can mainly be attributed to traps states at the buried interface of 2PACz/$FAPbI_3$ (Figures 3A–3C).

We next perform electrochemical impedance spectroscopy (EIS) to shed light on the charge carrier transport and recombination within the PSCs.[54,63,68] The Nyquist plots are obtained in the dark with an applied bias of 1 V close to V_{OC} as shown in Figure 3H, depicting two semicircles at the different frequency ranges (although another straight-like transmission line at the end of the low-frequency region is not considered for fitting and calculation as the charge carrier diffusion is neglected; more details can be found in the supplemental experimental procedures and Figure S12). In general, the high-frequency semicircle is related to the charge transport resistance (R_{tr}), and the low-frequency semicircle is ascribed to charge recombination resistance (R_{rec}) at the interfaces or within the bulk of the perovskite layer. Thus, we fit R_{tr} and R_{rec} with an equivalent circuit, as shown in Figure S12A. The smaller semicircle in the high frequency and larger semicircle in the low frequency for the VAG-30-s PSCs indicate lower R_{tr} (38.4 Ω) and higher R_{rec} (166.5 Ω), respectively (Figure 3H), compared with the AS-PSCs (R_{tr} = 53.9 Ω, R_{rec} = 66.7 Ω). This demonstrates improved charge transport and reduced recombination in the VAG-30-s PSCs. Further evidence for the reduced recombination is found in the variation of R_{rec} values with different applied biases (1–0 V, i.e., from open-circuit condition to short-circuit condition; Figures S12B–S12E). As shown in Figure S12F and Table S2, the VAG-30-s PSCs exhibit very high values of R_{rec} in the range of 4.4 × 10^4–4.6 × 10^7 Ω, whereas the values for the AS-PSCs are in the range of 452.8–747.0 Ω. All EIS data are in line with the above-discussed results (i.e., TRPL, PLQY, Mott-Schottky, dark *J-V*, light intensity dependent V_{OC}, and SCLC), demonstrating that the optimized VAG method effectively improves the buried interface with the elimination of interfacial voids and is thus beneficial for efficient charge transport and minimization of non-radiative recombination.

Having demonstrated that the enhanced V_{OC} is correlated to reduced non-radiative recombination due to the reduced number of voids in perovskite thin films processed via the VAG method, in the following, we study the effect of interfacial voids on the CE that relates rather to the J_{SC}. First, we perform CE measurements under different illumination intensities (1–100 mW cm^{-2}) to estimate the extracted charge carrier density (n_{CE}). As illustrated in Figure S13A, the PSC is illuminated at the open-circuit condition and consequently no current flows. At t = 0 s, the illumination is switched off, and simultaneously, a negative extraction voltage is applied. This way, nearly all excited charge carriers are extracted and induced a transient current. n_{CE} is determined by integrating

over the entire extracted current (see supplemental experimental procedures).[69–71] Compared with the AS-PSCs, we observe that more current is extracted for the VAG-30-s PSCs, especially under a low light intensity (<10 mW cm^{-2}) (Figures 4A and 4B), and the transient current instantaneously realizes the maximum value when the light intensity increases above 10 mW cm^{-2}. Overall, the calculated n_{CE} of the VAG-30-s PSCs is much higher than that of the AS-PSCs under varied illumination intensity (Figure 4B), revealing improved charge carrier extraction.

To further verify the improvement of charge carrier extraction within the VAG-30-s PSCs, we conduct delay-time CE by linearly increasing voltage (delay-time-CELIV) to understand the dynamic process of charge carrier extraction and recombination. Delay-time-CELIV has been established for organic solar cells[72–74] and PSCs.[75–77] As illustrated in Figure S13B, the PSCs are initially illuminated with a light intensity of 100 mW cm^{-2} at the open-circuit condition to impede any net current flow. The illumination is then switched off and PSCs are kept at open-circuit condition during the delay time. After the delay time, the linearly negative ramp voltage starts at $t = 0$ s. The calculation of charge carrier density (n_{CELIV}) can be found in the supplemental experimental procedures. As shown in Figure 4C, the AS-PSCs exhibit a single peak under all delay-timescales, but a wider peak under lower delay-timescales (<50 ns), where t is in the range of 5–11 μs, indicating that the extraction rate of the photogenerated charge carriers reaches its maximum during 5–11 μs (Figure S14A). In contrast, the VAG-30 s PSCs exhibit two peaks: $t < 2$ μs (Figure S14B) under a lower delay-timescale (<300 ns) reveals a rapid charge carrier extraction, and t in the range of 5–7 μs (Figure S14B) under a longer delay-timescale (300 ns–10 μs) indicates efficient extraction during 5–7 μs. We hypothesize that a longer delay time implies more charge carrier recombination and consequently less extraction. Therefore, we expect that under different delay-timescales, the calculated n_{CELIV} for the VAG-30-s PSCs is always much higher compared with the AS-PSCs (Figure 4D), which is in line with the trend in the CE data (Figure 4B). To summarize, the above data further indicate the enhancement of charge carrier extraction for the VAG-30 s PSCs.

We provide an illustration of the enhanced path length of charge carriers in the perovskite thin film in the presence of voids (Figure 4E). Assuming a void-free interface (as present for the condition VAG-30-s PSCs), photogenerated charge carriers (electrons or holes) can be extracted efficiently over the entire device area at the interface to the ETL or HTL (Figure 4A). This is reflected also in higher values in n_{CE} and n_{CELIV} for VAG-30-s PSCs (Figures 4B and 4D). However, if large amounts of voids are present at the perovskite/HTL interfaces (i.e., for the process conditions AS-, VAG-60-s, and VAG-120-s PSCs; Figures 2B and 2F), holes generated in the perovskite thin film above voids areas are required to travel a significantly enhanced path, which effectively reduces the charge carrier density (Figures 4B and 4D). Moreover, the large voids in the buried interface accumulate trap states at the surface (Figure 3G),[17,46] which will trap charge carriers (mostly holes in our *p-i-n* PSCs) (Figure 4E). For these reasons, a higher void ratio leads to a lower J_{SC} and V_{OC} within devices due to poor CE and increased non-radiative recombination (Figure 2F).

Finally, having discussed and demonstrated the advantages of the VAG method in laboratory-scale PSCs processed with the VAG method, we demonstrate the fabrication of PSCs and modules using fully scalable deposition methods (blade coating for 2PACz and $FAPbI_3$ layers, vacuum deposition for C_{60}, Au, and MgF_2) on larger-area substrates. The key challenge for large-area blade coating is to obtain continual and homogeneous perovskite thin films free of interfacial voids. For small-area spin-coated PSCs, the centrifugal force during the spin-coating process already

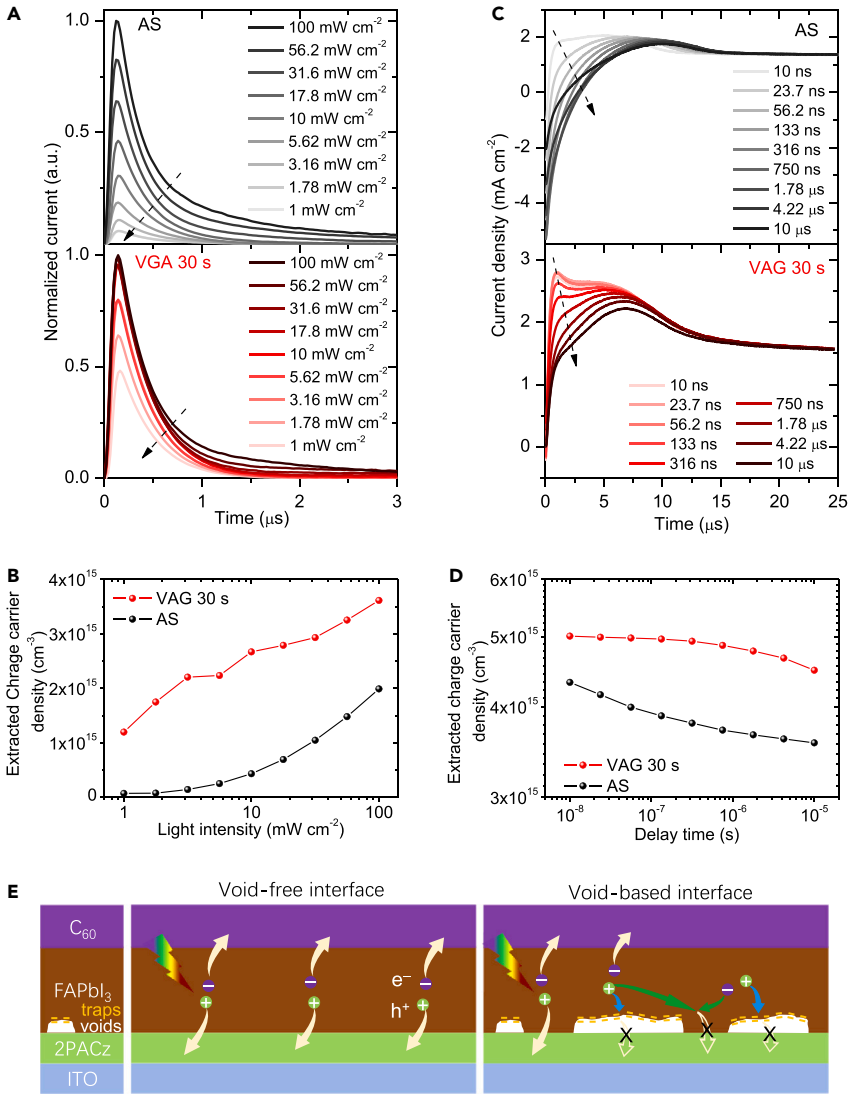

Figure 4. Characteristics of charge extraction

(A and B) (A) Transient current and (B) extracted charge carrier density derived from charge extraction (CE) measurement under variable illumination intensities (1–100 mW cm^{-2}).

(C and D) (C) Transient current density vs. time profiles and (D) extracted charge carrier density with different delay time derived from delay-time-CELIV characterization at light intensity of 100 mW cm^{-2}.

(E) Schematic of the charge extraction process in PSCs with void-free and void-based interfaces.

assists in removing most of the precursor solution, thus evaporating most of the solvents before the VAG step. However, the blade-coating process has an intrinsic longer drying time; thus, it is challenging when the deposited perovskite ink is naturally dried out without additional treatments. For the blade-coated wet film of perovskite, it takes several tens of minutes to obtain the solid-state dried film during the VAG step. As discussed above, a longer vacuum time leads to a large number of interfacial voids. Thus, we developed a nitrogen-flow-combined VAG (N_2-VAG) to accelerate the solvent extraction that has already been employed in our latest work.[15] The fabrication of $FAPbI_3$ thin films (on 6.4 × 3.2 cm^2 substrate) is illustrated in Figure 5A. We observe considerable white spots in control films (without N_2 flow and without additives) visualized from the glass side (Figures 5B and S15). These spots with

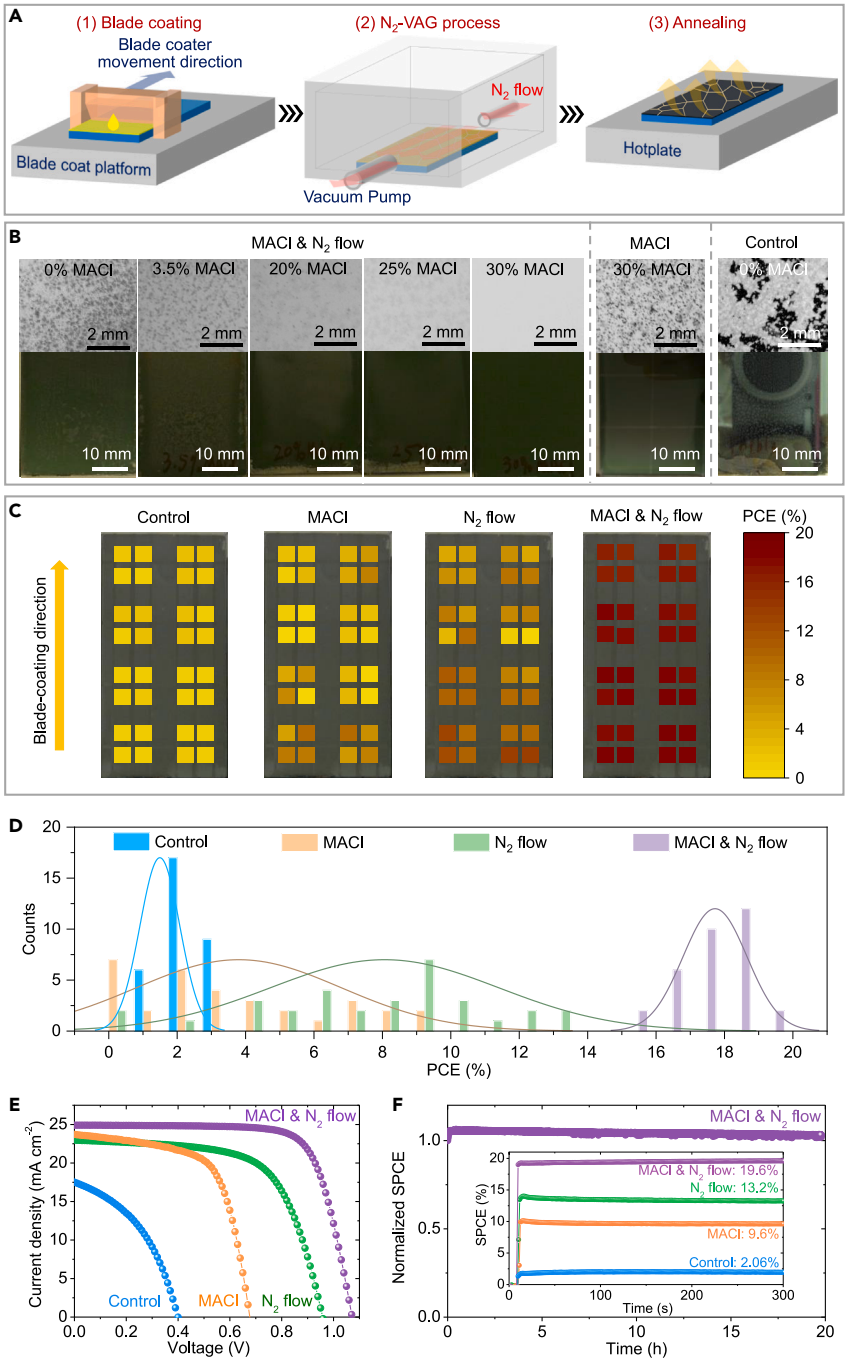

Figure 5. Blade-coated perovskite thin films and scalable PSCs

(A) Schematic of perovskite fabrication of the combination of blade coating and vacuum-assisted growth applying a moderate N_2 flow (N_2-VAG).

(B) Photographs and optical microscopic images of the glass side for bade-coated $FAPbI_3$ thin films (substrate dimension: 6.4 × 3.2 cm^2). The white region in photographs as well as dark region in microscopic images indicates voids.

(C and D) (C) The heatmap and (D) statistical distribution of power conversion efficiency (PCE).

(E and F) (E) Current density-voltage (*J-V*) characteristics and (F) stabilized power conversion efficiency (SPCE) under continuous illumination for the best-performing PSCs (with MgF_2 antireflection coating).

millimeter dimensions are discussed as voids at the buried interface of HTL/$FAPbI_3$, which are larger compared with the spin-coated thin films due to the intrinsic low rate of nucleation and crystallization without any treatments. This demonstrates that these voids are easily produced in the blade-coating process on larger substrates. After the N_2 flow is introduced (without any additives), the size of voids reduces; however, they do not disappear (Figure S15). Thus, we realize that the N_2-VAG route is not sufficient for obtaining obtain high-quality $FAPbI_3$ thin films free of voids. To resolve this problem, we incorporate an optimized amount of 30 mol % MACl in the perovskite precursor combined with N_2 flow (referred to as MACl and N_2 flow), thus obtaining a high-quality homogeneous and void-free thin film (Figures 5B, S15, and S16). It was previously demonstrated that precursor compositions with MACl induce an intermediate phase during the early drying stage and nucleation phase and further promote the film growth of secondary crystallization during annealing process, thus facilitating the growth of homogeneous $FAPbI_3$ thin films.[7,17] Consequently, we employ MACl here to further improve the film quality in the blade-coated large-area devices. We note that a lower concentration (<30 mol %) of MACl also leads to an inhomogeneous blade-coated thin film with numerous interfacial voids (Figures 5B, S15, and S16). We observe the same phenomenon in the spin-coated small-area PSCs (Figure S17) for varying MACl concentrations. We note that utilizing 30 mol % MACl in the absence of a N_2 flow still generates voids at the interface (Figures 5B, S15, and S16). To accelerate the extraction of solvents in the VAG step, we regulate and optimize the N_2 flow (~180 cm^3 min^{-1}, Figures S18 and S19) and the vacuum time (~30 s) for processing on the large-area substrates (Figures S19–S21). Importantly, insufficient, or too high N_2 flow results in a large density of voids and produces inhomogeneous thin films (Figure S19B). An optimal rate of solvent extraction from the N_2 flow improves the nucleation and crystallization to form an intermediate phase that facilitates the growth of the α-phase during the thermal annealing process. We conclude that the absence of MACl or N_2 flow leads to a large number of voids, pinholes, and low coverage (Figures S15, S19B, and S20). We further demonstrate that the employing introduced a combination of MACl as an additive and N_2 flow produces high-quality void-free $FAPbI_3$ thin films on different HTLs, e.g., NiO_x, poly(3,4-ethylenedioxythiophene)-poly(styrenesulfonate) (PEDOT:PSS), and poly[bis(4-phenyl)(2,4,6-trimethylphenyl)amine] (PTAA) (Figure S21). In summary, we realize the fabrication of high-quality, continual, and homogeneous blade-coated large-area $FAPbI_3$ thin films via an optimized MACl and N_2-flow route that is an effective approach for upscaling perovskite photovoltaics on different HTLs (Figures S20 and S21).

We evaluate the PCE distribution of the divided PSCs that are processed with large substrates (the 6.4 × 3.2 cm^2 substrate is divided into 32 pieces of samples with dimensions 1.6 × 1.6 cm^2). To avoid any de-wetting issue of the perovskite precursor on the etched area of ITO/2PACz large substrates (the width of the etch lines is equal to 1.5 mm), we employed a 5 nm sputtered NiO_x thin film beneath 2PACz (Figure S21) and maintain otherwise the same architecture as the optimized spin-coated PSCs. The heatmap in Figure 5C reflects the distribution of PCEs for each blade-coated PSC processed at different positions of the large substrate. It is apparent that all control PSCs (no N_2 flow and no MACl) present very low PCE below 3% due to numerous voids and low coverage of $FAPbI_3$ on top of ITO/NiO_x/2PACz substrates (Figures S15 and S20). Either the MACl-only or N_2-flow-only route enhances the device performance, but their PCEs are still less than 15% with a large variation (Figure 5D). The low V_{OC} and FF are the main limitations of the device performance (Figure S22), which we attribute to the severe non-radiative recombination loss due to the interfacial voids. Simultaneously, MACl-only or N_2-flow-only route may trigger

a large variation in film thickness (Figure S23) or inhomogeneous films with voids (Figures 5B, S15, and S16) for blade-coating process owing to the unregulated crystallization, thus resulting in low reproducibility and yield (Figures 5C and 5D). In contrast, the optimized MACl and N_2-flow route allows us to obtain high yield and PCEs (Figures 5C and 5D). The best-performing PSC with MgF_2 antireflection coating delivers an excellent PCE of 20.0%, with a FF of 0.75, V_{OC} of 1.07 V, and J_{SC} of 24.9 mA cm^{-2} (Figure 5E; Table S3), which is much higher than the control PSCs (PCE = 2.9%), and PSCs processed with MACl (PCE = 10.3%) and N_2-flow (PCE = 14.1%) routes. The integrated J_{SC} of 24.2 mA cm^{-2} extracted from EQE (Figure S24) matches well with the value from the *J-V* measurement. Furthermore, the best-performing PSC fabricated via MACl and N_2 flow route also delivers an impressive SPCE of up to 19.6% at MPP tracking under continuous AM 1.5G irradiation for 20 h (Figure 5F).

Finally, we present fully scalable *p-i-n*-based $FAPbI_3$ perovskite solar mini-modules. The modules employ the same architecture and upscaling methods as discussed above. Figures 6A and 6B show an all-laser-scribed module (processed with fully scalable deposition methods), comprising seven monolithically interconnected sub-cells with an aperture area of 12.25 cm^2 (Figure S25A).[78] The widths of the scribing lines P1, P2, and P3 are 44, 50, and 28 μm, respectively (Figure 6C). Considering the total width of 184 μm for the dead area, we estimate a GFF of 96.3% (Figure S25B). Compared with other single-junction or 2T-all-perovskite tandem solar modules,[14,15,45,62,79] we significantly enhance the realized GFF by optimizing the electrical properties of all scribing lines at minimal width and improving their respective alignment.[78] The best-performing mini-module with MgF_2 antireflection coating delivers a PCE of 18.3% (Figures 6D and S26; Table S4, V_{OC} = 7.36 V, short-circuit current I_{sc} = 41.2 mA, and FF = 0.74). The best-performing sub-cell in the module (active area of 1.69 cm^2) presents an active-area efficiency of 19.8% (Figure S27) that demonstrates a low efficiency loss of ~7% in upscaling. This reveals a successful interconnection design and laser scribing while upscaling the modules. Furthermore, it is worth to note that we realized a noticeable low efficiency loss of ~1% in a larger active-area fabrication of blade-coated PSCs (PCE = 19.8% for 1.69 cm^2, Figure S27) compared with our reference blade-coated smaller PSCs (PCE = 20.0% for 0.105 cm^2, Figure 5E). The average V_{OC} contribution of each sub-cell is ~1.05 V (Table S4). This value is comparable with that obtained from the blade-coated small PSCs (1.07 V for 0.105 cm^2, Table S3), indicating negligible voltage loss for the employed upscaling process. Simultaneously, the module retains a high I_{sc} of 41.2 mA, demonstrating a good current collection of the introduced module interconnections compared with different sub-cells in series showing 41.3–41.5 mA (Table S4). Moreover, our module presents a good SPCE of up to 18.0% at MPP tracking under continuous AM 1.5G irradiation and stabilizes at 85°C in an inert atmosphere for 20 h (Figure 6E). Next, we evaluate the stability of our $FAPbI_3$ PSCs against moisture. It is observed that AS-$FAPbI_3$ thin films degrade faster compared with VAG-$FAPbI_3$ thin films (Figure S28) stored in air (temperature ~19°C, relative humidity [RH] ~ 60%). After 11-day storage, AS-$FAPbI_3$ thin films exhibit degradation along with numerous voids, whereas VAG-$FAPbI_3$ thin film shows less degradation and almost no voids (Figure S29). After 15 days, a severe degradation with yellowish regions (Figures S28 and S29) is present in AS-$FAPbI_3$ thin films. In line with literature, we attribute the yellow regions to phase transitions due to the emergence of the δ-phase.[18–20] We further test the device stability at a higher RH of 85% and an elevated temperature (85°C) in a climate chamber (Figure S30A). However, all $FAPbI_3$- and $Cs_{0.18}FA_{0.82}PbI_3$-based thin films or PSCs fabricated with AS and VAG process degrade within less than 30 min (Figures S30B and S30C). We conclude that the developed VAG process delivers good thermal stability and enhanced phase stability compared with the reference AS quenching method.

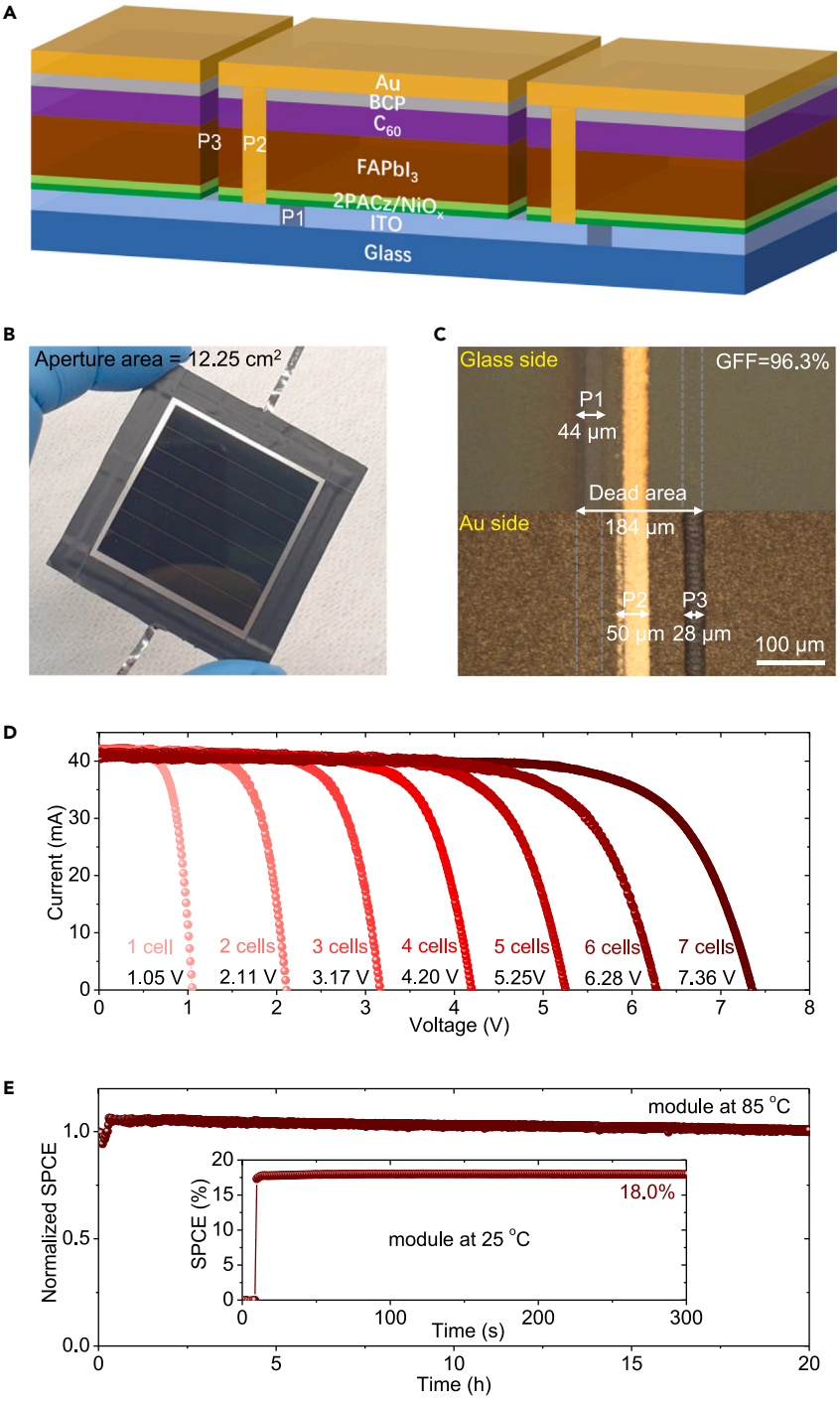

Figure 6. Scribing lines and scalable modules

(A) Schematic diagram of $FAPbI_3$ perovskite solar module interconnected by scribing lines.

(B) Photograph of the glass side of the module (dimension: 5.0 × 5.0 cm^2).

(C) Optical microscopic images of the module from the glass and Au sides (top metal contact).

(D and E) (D) Current density-voltage (*J-V*) characteristics and (E) stabilized power conversion efficiency (SPCE) under AM 1.5G continuous illumination at 85°C and 25°C (inset) in N_2-filled glovebox for the best-performing module (with MgF_2 antireflection coating).

However, advancing further the stability of $FAPbI_3$ thin films toward a high level of moisture as well as good encapsulation is pivotal for the progress of $FAPbI_3$-based perovskite photovoltaics.

Conclusions

We successfully demonstrate high-efficiency *p-i-n*-based $FAPbI_3$ PSCs and modules processed with scalable fabrication methods. Using the VAG process with optimized vacuum time (30 s) facilitates void-free spin-coated $FAPbI_3$ thin films, compared with the reference AS method that shows interfacial voids at the 2PACz/$FAPbI_3$ interface. We present a champion PCE of 22.3% with improved V_{OC} and J_{SC}. Our observations based on TRPL, Mott-Schottky, PLQY, EIS, and SCLC analyses demonstrate that the V_{OC} improvement originates from reduced non-radiative recombination at the buried interface of 2PACz/$FAPbI_3$. CE and delay-time-CELIV reveal the enhancement of CE that enables a higher J_{SC}. Finally, we further develop an optimized MACl and N_2-flow route to fabricate high-quality, void-free, large-area, blade-coated $FAPbI_3$ thin films, achieving highly efficient blade-coated PSCs and mini-modules (aperture area of 12.25 cm^2) with good PCEs of 20.0% and 18.3%, respectively.

EXPERIMENTAL PROCEDURES

Resource availability

Lead contact

Further information and requests for resources should be directed to and will be fulfilled by the lead contact, Bahram Abdollahi Nejand (bahram.abdollahi@kit.edu).

Materials availability

This study did not generate new unique materials.

Data and code availability

This study did not generate any unique datasets or code.

ACKNOWLEDGMENTS

Financial support from the Initiating and Networking funding of Helmholtz Association HYIG of U.W.P. (VH-NG-1148), the Helmholtz Energy Materials Foundry (HEMF), and Karlsruhe School of Optics and Photonics (KSOP) is gratefully acknowledged. The authors acknowledge the Helmholtz Association (program-oriented funding IV, Materials and Technologies for the Energy Transition, Topic 1: Photovoltaics and Wind Energy, Code: 38.01.02). B.A.N. acknowledges the financial support from the European Union's Horizon 2020 research and innovation program under the Marie Skłodowska-Curie (grant agreement no. 840937). H.H. acknowledges the Chinese Scholarship Council (CSC, no. 201808420221) for funding his doctoral research work.

AUTHOR CONTRIBUTIONS

H.H., U.W.P., and B.A.N. conceived the idea and designed the experiments. H.H. did the fabrication of PSCs and modules, the rest of characterizations, and data

analysis. D.B.R. conducted the laser scribing for modules. A.D. performed SEM. Y.L. conducted TRPL. R.S. conducted XRD and stability testing. P.F. performed PLQY and data analysis. Q.J. performed AFM and contact angle measurements. F.S. and B.A.N. supported the vacuum-quenching system construction. U.W.P. and B.A.N. supervised the project. All authors were involved in the discussions and input of writing the manuscript.

DECLARATION OF INTERESTS

The authors declare no competing interests.

REFERENCES

1. NREL National Center for Photovoltaics (2022). Best research-cell efficiency chart. https://www.nrel.gov/pv/cell-efficiency.html.
2. Eperon, G.E., Stranks, S.D., Menelaou, C., Johnston, M.B., Herz, L.M., and Snaith, H.J. (2014). Formamidinium lead trihalide: A broadly tunable perovskite for efficient planar heterojunction solar cells. Energy Environ. Sci. *7*, 982–988.
3. Lee, J.W., Seol, D.J., Cho, A.N., and Park, N.G. (2014). High-efficiency perovskite solar cells based on the black polymorph of HC(NH2) 2PbI3. Adv. Mater. *26*, 4991–4998.
4. Conings, B., Drijkoningen, J., Gauquelin, N., Babayigit, A., d'haen, J., D'Olieslaeger, L., Ethirajan, A., Verbeeck, J., Manca, J., Mosconi, E., et al. (2015). Intrinsic thermal instability of methylammonium lead trihalide perovskite. Adv. Energy Mater. *5*, 1–6.
5. Min, H., Kim, M., Lee, S.U., Kim, H., Kim, G., Choi, K., Lee, J.H., and Seok, S.I., Il (2019). Efficient, stable solar cells by using inherent bandgap of a-phase formamidinium lead iodide. Science *366*, 749–753.
6. Lu, H., Liu, Y., Ahlawat, P., Mishra, A., Tress, W.R., Eickemeyer, F.T., Yang, Y., Fu, F., Wang, Z., Avalos, C.E., et al. (2020). Vapor-assisted deposition of highly efficient, stable black-phase FAPbI3 perovskite solar cells. Science *370*, eabb8985. https://doi.org/10.1126/science.abb8985.
7. Kim, M., Kim, G.H., Lee, T.K., Choi, I.W., Choi, H.W., Jo, Y., Yoon, Y.J., Kim, J.W., Lee, J., Huh, D., et al. (2019). Methylammonium chloride induces intermediate phase stabilization for efficient perovskite solar cells. Joule *3*, 2179–2192.
8. Jeong, M., Choi, I.W., Go, E.M., Cho, Y., Kim, M., Lee, B., Jeong, S., Jo, Y., Choi, H.W., Lee, J., et al. (2020). Stable perovskite solar cells with efficiency exceeding 24.8% and 0.3-V voltage loss. Science *369*, 1615–1620.
9. Hui, W., Chao, L., Lu, H., Xia, F., Wei, Q., Su, Z., Niu, T., Tao, L., Du, B., Li, D., et al. (2021). Stabilizing black-phase formamidinium perovskite formation at room temperature and high humidity. Science *371*, 1359–1364.
10. Jeong, J., Kim, M., Seo, J., Lu, H., Ahlawat, P., Mishra, A., Yang, Y., Hope, M.A., Eickemeyer, F.T., Kim, M., et al. (2021). Pseudo-halide anion engineering for α-FAPbI3 perovskite solar cells. Nature *592*, 381–385.
11. Min, H., Lee, D.Y., Kim, J., Kim, G., Lee, K.S., Kim, J., Paik, M.J., Kim, Y.K., Kim, K.S., Kim, M.G., et al. (2021). Perovskite solar cells with atomically coherent interlayers on SnO2 electrodes. Nature *598*, 444–450.
12. Lin, R., Xu, J., Wei, M., Wang, Y., Qin, Z., Liu, Z., Wu, J., Xiao, K., Chen, B., Park, S.M., et al. (2022). All-perovskite tandem solar cells with improved grain surface passivation. Nature *603*, 73–78.
13. Deng, Y., Zheng, X., Bai, Y., Wang, Q., Zhao, J., and Huang, J. (2018). Surfactant-controlled ink drying enables high-speed deposition of perovskite films for efficient photovoltaic modules. Nat. Energy *3*, 560–566.
14. Xiao, K., Lin, Y.H., Zhang, M., Oliver, R.D.J., Wang, X., Liu, Z., Luo, X., Li, J., Lai, D., Luo, H., et al. (2022). Scalable processing for realizing 21.7%-efficient all-perovskite tandem solar modules. Science *376*, 762–767.
15. Abdollahi Nejand, B., Ritzer, D.B., Hu, H., Schackmar, F., Moghadamzadeh, S., Feeney, T., Singh, R., Laufer, F., Schmager, R., Azmi, R., et al. (2022). Scalable two-terminal all-perovskite tandem solar modules with a 19.1% efficiency. Nat. Energy *7*, 620–630.
16. Du, T., Macdonald, T.J., Yang, R.X., Li, M., Jiang, Z., Mohan, L., Xu, W., Su, Z., Gao, X., Whiteley, R., et al. (2022). Additive-free, low-temperature crystallization of stable α-FAPbI3 perovskite. Adv. Mater. *34*, 1–10.
17. Zhang, D., Zhang, H., Guo, H., Ye, F., Liu, S., and Wu, Y. (2022). Stable α-FAPbI3 in inverted perovskite solar cells with efficiency exceeding 22% via a self-passivation strategy. Adv. Funct. Mater. *32*, 2200174.
18. Song, Z., Abate, A., Watthage, S.C., Liyanage, G.K., Phillips, A.B., Steiner, U., Graetzel, M., and Heben, M.J. (2016). Perovskite solar cell stability in humid air: partially reversible phase transitions in the PbI2-CH3NH3I-H2O system. Adv. Energy Mater. *6*, 1600846.
19. Chen, H., Chen, Y., Zhang, T., Liu, X., Wang, X., and Zhao, Y. (2021). Advances to high-performance black-phase FAPbI 3 perovskite for efficient and stable photovoltaics. Small Struct. *2*, 2000130.
20. Fu, C., Gu, Z., Tang, Y., Xiao, Q., Zhang, S., Zhang, Y., and Song, Y. (2022). From structural design to functional construction: amine molecules in high-performance formamidinium-based perovskite solar cells. Angew. Chem. Int. Ed. Engl. *61*, e202117067.
21. Wang, F., Yu, H., Xu, H., and Zhao, N. (2015). HPbI3: A new precursor compound for highly efficient solution-processed perovskite solar cells. Adv. Funct. Mater. *25*, 1120–1126.
22. Zhou, Z., Pang, S., Ji, F., Zhang, B., and Cui, G. (2016). The fabrication of formamidinium lead iodide perovskite thin films via organic cation exchange. Chem. Commun. (Camb) *52*, 3828–3831.
23. Ke, W., Spanopoulos, I., Stoumpos, C.C., and Kanatzidis, M.G. (2018). Myths and reality of HPbI3 in halide perovskite solar cells. Nat. Commun. *9*, 4785.
24. Bian, H., Wang, H., Li, Z., Zhou, F., Xu, Y., Zhang, H., Wang, Q., Ding, L., Liu, S.F., and Jin, Z. (2020). Unveiling the effects of hydrolysis-derived DMAI/DMAPbIx intermediate compound on the performance of CsPbI3 solar cells. Adv. Sci. (Weinh) *7*, 1902868.
25. Lee, J.W., Dai, Z., Lee, C., Lee, H.M., Han, T.H., De Marco, N., Lin, O., Choi, C.S., Dunn, B., Koh, J., et al. (2018). Tuning molecular interactions for highly reproducible and efficient formamidinium perovskite solar cells via adduct approach. J. Am. Chem. Soc. *140*, 6317–6324.
26. Shen, C., Wu, Y., Zhang, S., Wu, T., Tian, H., Zhu, W.H., and Han, L. (2020). Stabilizing formamidinium lead iodide perovskite by sulfonyl-functionalized Phenethylammonium salt via crystallization control and surface passivation. Sol. RRL *4*, 1–7.
27. Lee, J.W., Dai, Z., Han, T.H., Choi, C., Chang, S.Y., Lee, S.J., De Marco, N., Zhao, H., Sun, P., Huang, Y., et al. (2018). 2D perovskite stabilized

phase-pure formamidinium perovskite solar cells. Nat. Commun. *9*, 3021.

28. Yang, S., Liu, W., Zuo, L., Zhang, X., Ye, T., Chen, J., Li, C.Z., Wu, G., and Chen, H. (2016). Thiocyanate assisted performance enhancement of formamidinium based planar perovskite solar cells through a single one-step solution process. J. Mater. Chem. A *4*, 9430–9436.

29. Alanazi, A.Q., Kubicki, D.J., Prochowicz, D., Alharbi, E.A., Bouduban, M.E.F., Jahanbakhshi, F., Mladenović, M., Milić, J.V., Giordano, F., Ren, D., et al. (2019). Atomic-level microstructure of efficient formamidinium-based perovskite solar cells stabilized by 5-ammonium valeric acid iodide revealed by multinuclear and two-dimensional solid-state NMR. J. Am. Chem. Soc. *141*, 17659–17669.

30. Masi, S., Echeverría-Arrondo, C., Salim, K.M.M., Ngo, T.T., Mendez, P.F., López-Fraguas, E., Macias-Pinilla, D.F., Planelles, J., Climente, J.I., and Mora-Seró, I. (2020). Chemi-structural stabilization of formamidinium lead iodide perovskite by using embedded quantum dots. ACS Energy Lett. *5*, 418–427.

31. Saliba, M., Matsui, T., Domanski, K., Seo, J.Y., Ummadisingu, A., Zakeeruddin, S.M., Correa-Baena, J.P., Tress, W.R., Abate, A., Hagfeldt, A., et al. (2016). Incorporation of rubidium cations into perovskite solar cells improves photovoltaic performance. Science *354*, 206–209.

32. Saliba, M., Matsui, T., Seo, J.Y., Domanski, K., Correa-Baena, J.P., Nazeeruddin, M.K., Zakeeruddin, S.M., Tress, W., Abate, A., Hagfeldt, A., et al. (2016). Cesium-containing triple cation perovskite solar cells: improved stability, reproducibility and high efficiency. Energy Environ. Sci. *9*, 1989–1997.

33. Zhang, M., Yun, J.S., Ma, Q., Zheng, J., Lau, C.F.J., Deng, X., Kim, J., Kim, D., Seidel, J., Green, M.A., et al. (2017). High-efficiency rubidium-incorporated perovskite solar cells by gas quenching. ACS Energy Lett. *2*, 438–444.

34. Son, D.Y., Kim, S.G., Seo, J.Y., Lee, S.H., Shin, H., Lee, D., and Park, N.G. (2018). Universal approach toward hysteresis-free perovskite solar cell via defect engineering. J. Am. Chem. Soc. *140*, 1358–1364.

35. Kim, G., Min, H., Lee, K.S., Lee, D.Y., Yoon, S.M., and Seok, S.I., Il (2020). Impact of strain relaxation on performance of a-formamidinium lead iodide perovskite solar cells. Science *370*, 108–112.

36. Luo, W., Wu, C., Wang, D., Zhang, Y., Zhang, Z., Qi, X., Zhu, N., Guo, X., Qu, B., Xiao, L., et al. (2019). Efficient and stable perovskite solar cell with high open-circuit voltage by dimensional interface modification. ACS Appl. Mater. Interfaces *11*, 9149–9155.

37. Wang, F., Geng, W., Zhou, Y., Fang, H.H., Tong, C.J., Loi, M.A., Liu, L.M., and Zhao, N. (2016). Phenylalkylamine passivation of organolead halide perovskites enabling high-efficiency and air-stable photovoltaic cells. Adv. Mater. *28*, 9986–9992.

38. Liu, Y., Akin, S., Hinderhofer, A., Eickemeyer, F.T., Zhu, H., Seo, J.Y., Zhang, J., Schreiber, F., Zhang, H., Zakeeruddin, S.M., et al. (2020). Stabilization of highly efficient and stable phase-pure FAPbI3 perovskite solar cells by molecularly tailored 2D-overlayers. Angew. Chem. Int. Ed. Engl. *59*, 15688–15694.

39. Li, G., Zhang, T., Xu, F., and Zhao, Y. (2017). A facile deposition of large grain and phase pure a-FAPbI3 for perovskite solar cells via a flash crystallization. Mater. Today Energy *5*, 293–298.

40. Meng, L., Sun, C., Wang, R., Huang, W., Zhao, Z., Sun, P., Huang, T., Xue, J., Lee, J.W., Zhu, C., et al. (2018). Tailored phase conversion under conjugated polymer enables thermally stable perovskite solar cells with efficiency exceeding 21%. J. Am. Chem. Soc. *140*, 17255–17262.

41. Xie, F., Chen, C.C., Wu, Y., Li, X., Cai, M., Liu, X., Yang, X., and Han, L. (2017). Vertical recrystallization for highly efficient and stable formamidinium-based inverted-structure perovskite solar cells. Energy Environ. Sci. *10*, 1942–1949.

42. Xu, Z., Zeng, L., Hu, J., Wang, Z., Zhang, P., Brabec, C.J., Forberich, K., Mai, Y., and Guo, F. (2022). Reducing energy barrier of δ-to-α phase transition for printed formamidinium lead iodide photovoltaic devices. Nano Energy *91*, 106658.

43. Dai, Z., Yadavalli, S.K., Chen, M., Abbaspourtamijani, A., Qi, Y., and Padture, N.P. (2021). Interfacial toughening with self-Assembled monolayers enhances perovskite solar cell reliability. Science *372*, 618–622.

44. Dong, Q., Zhu, C., Chen, M., Jiang, C., Guo, J., Feng, Y., Dai, Z., Yadavalli, S.K., Hu, M., Cao, X., et al. (2021). Interpenetrating interfaces for efficient perovskite solar cells with high operational stability and mechanical robustness. Nat. Commun. *12*, 973.

45. Chen, S., Dai, X., Xu, S., Jiao, H., Zhao, L., and Huang, J. (2021). Stabilizing perovskite-substrate interfaces for high-performance perovskite modules. Science *373*, 902–907.

46. Yang, X., Luo, D., Xiang, Y., Zhao, L., Anaya, M., Shen, Y., Wu, J., Yang, W., Chiang, Y.H., Tu, Y., et al. (2021). Buried interfaces in halide perovskite photovoltaics. Adv. Mater. *33*, e2006435.

47. Zhou, Y., Kwun, J., Garces, H.F., Pang, S., and Padture, N.P. (2016). Observation of phase-retention behavior of the HC(NH2)2PbI3 black perovskite polymorph upon mesoporous TiO2 scaffolds. Chem. Commun. (Camb) *52*, 7273–7275.

48. He, W., Hu, J., Chen, C., Chen, Y., Zeng, L., Zhang, X., Cai, B., Mai, Y., and Guo, F. (2020). Temperature-assisted crystal growth of photovoltaic α-phase FAPbI3 thin films by sequential blade coating. ACS Appl. Mater. Interfaces *12*, 55830–55837.

49. Liang, Q., Liu, K., Sun, M., Ren, Z., Fong, P.W.K., Huang, J., Qin, M., Wu, Z., Shen, D., Lee, C.S., et al. (2022). Manipulating crystallization kinetics in high-performance blade-coated perovskite solar cells via cosolvent-assisted phase transition. Adv. Mater. *34*, e2200276.

50. Lee, D., Jeong, D., Ahn, T.K., and Park, N. (2019). Precursor Engineering for a Large-Area perovskite Solar Cell with >19% E ffi ciency. ACS Energy Lett. *4*, 2393–2401.

51. Deng, Y., Brackle, C.H. Van, Dai, X., Zhao, J., Chen, B., and Huang, J. (2019). Tailoring solvent coordination for high-speed , room-temperature blading of perovskite photovoltaic films. Sci. Adv. *5*, eaax7537.

52. Fong, P.W., Hu, H., Ren, Z., Liu, K., Cui, L., Bi, T., and Liang, Q. (2021). Printing high-efficiency perovskite solar cells in high-humidity ambient environment — an in situ guided investigation. Adv. Sci. *8*, 2003359.

53. Abdollahi Nejand, B., Hossain, I.M., Jakoby, M., Moghadamzadeh, S., Abzieher, T., Gharibzadeh, S., Schwenzer, J.A., Nazari, P., Schackmar, F., Hauschild, D., et al. (2020). Vacuum-assisted growth of low-bandgap thin films (FA 0.8 MA 0.2 Sn 0.5 Pb 0.5 I 3) for All-Perovskite Tandem Solar Cells. Adv. Energy Mater. *10*, 1902583.

54. Hu, H., Moghadamzadeh, S., Azmi, R., Li, Y., Kaiser, M., Fischer, J.C., Jin, Q., Maibach, J., Hossain, I.M., Paetzold, U.W., et al. (2022). Sn-Pb mixed perovskites with fullerene-derivative interlayers for efficient four-terminal all-perovskite tandem solar cells. Adv. Funct. Mater. *32*, 2107650.

55. Yoo, J.J., Seo, G., Chua, M.R., Park, T.G., Lu, Y., Rotermund, F., Kim, Y.K., Moon, C.S., Jeon, N.J., Correa-Baena, J.P., et al. (2021). Efficient perovskite solar cells via improved carrier management. Nature *590*, 587–593.

56. Liu, X., Lin, F., Chueh, C.C., Chen, Q., Zhao, T., Liang, P.W., Zhu, Z., Sun, Y., and Jen, A.K.Y. (2016). Fluoroalkyl-substituted fullerene/perovskite heterojunction for efficient and ambient stable perovskite solar cells. Nano Energy *30*, 417–425.

57. Liang, P.W., Chueh, C.C., Williams, S.T., and Jen, A.K.Y. (2015). Roles of fullerene-based interlayers in enhancing the performance of organometal perovskite thin-film solar cells. Adv. Energy Mater. *5*, 1–6.

58. Zuo, L., Chen, Q., De Marco, N., Hsieh, Y.T., Chen, H., Sun, P., Chang, S.Y., Zhao, H., Dong, S., and Yang, Y. (2017). Tailoring the interfacial chemical interaction for high-efficiency perovskite solar cells. Nano Lett. *17*, 269–275.

59. Gharibzadeh, S., Fassl, P., Hossain, I.M., Rohrbeck, P., Frericks, M., Schmidt, M., Duong, T., Khan, M.R., Abzieher, T., Nejand, B.A., et al. (2021). Two birds with one stone: dual grain-boundary and interface passivation enables >22% efficient inverted methylammonium-free perovskite solar cells. Energy Environ. Sci. *14*, 5875–5893.

60. Stolterfoht, M., Grischek, M., Caprioglio, P., Wolff, C.M., Gutierrez-Partida, E., Peña-Camargo, F., Rothhardt, D., Zhang, S., Raoufi, M., Wolansky, J., et al. (2020). How to quantify the efficiency potential of neat perovskite films: perovskite semiconductors with an implied efficiency exceeding 28%. Adv. Mater. *32*, e2000080.

61. Jung, E.H., Jeon, N.J., Park, E.Y., Moon, C.S., Shin, T.J., Yang, T.Y., Noh, J.H., and Seo, J. (2019). Efficient, stable and scalable perovskite solar cells using poly(3-hexylthiophene). Nature *567*, 511–515.

62. Zhu, J., Park, S., Gong, O.Y., Sohn, C.H., Li, Z., Zhang, Z., Jo, B., Kim, W., Han, G.S., Kim, D.H., et al. (2021). Formamidine disulfide oxidant as a localised electron scavenger for >20%

perovskite solar cell modules. Energy Environ. Sci. *14*, 4903–4914.

63. Bu, T., Li, J., Zheng, F., Chen, W., Wen, X., Ku, Z., Peng, Y., Zhong, J., Cheng, Y.B., and Huang, F. (2018). Universal passivation strategy to slot-die printed SnO 2 for hysteresis-free efficient flexible perovskite solar module. Nat. Commun. *9*, 4609.

64. Lin, R., Xiao, K., Qin, Z., Han, Q., Zhang, C., Wei, M., Saidaminov, M.I., Gao, Y., Xu, J., Xiao, M., et al. (2019). Monolithic all-perovskite tandem solar cells with 24.8% efficiency exploiting comproportionation to suppress Sn(ii) oxidation in precursor ink. Nat. Energy *4*, 864–873.

65. Shi, D., Adinolfi, V., Comin, R., Yuan, M., Alarousu, E., Buin, A., Chen, Y., Hoogland, S., Rothenberger, A., Katsiev, K., et al. (2015). Solar cells. Low trap-state density and long carrier diffusion in organolead trihalide perovskite single crystals. Science *347*, 519–522.

66. Akin, S., Akman, E., and Sonmezoglu, S. (2020). FAPbI3-based perovskite solar cells employing hexyl-based ionic liquid with an efficiency over 20% and excellent long-term stability. Adv. Funct. Mater. *30*, 2002964.

67. Han, Q., Bae, S.H., Sun, P., Hsieh, Y.T., Yang, Y.M., Rim, Y.S., Zhao, H., Chen, Q., Shi, W., Li, G., et al. (2016). Single crystal formamidinium lead iodide (FAPbI3): insight into the structural, optical, and electrical properties. Adv. Mater. *28*, 2253–2258.

68. Hu, H., Dong, B., Hu, H., Chen, F., Kong, M., Zhang, Q., Luo, T., Zhao, L., Guo, Z., Li, J., et al. (2016). Atomic layer deposition of TiO2 for a high-efficiency hole-blocking layer in hole-conductor-free perovskite solar cells processed in ambient air. ACS Appl. Mater. Interfaces *8*, 17999–18007.

69. Sandberg, O.J., Tvingstedt, K., Meredith, P., and Armin, A. (2019). Theoretical perspective on transient photovoltage and charge extraction techniques. J. Phys. Chem. C *123*, 14261–14271.

70. Tran, H.N., Park, S., Wibowo, F.T.A., Krishna, N.V., Kang, J.H., Seo, J.H., Nguyen-Phu, H., Jang, S.Y., and Cho, S. (2020). 17% non-fullerene organic solar cells with annealing-free aqueous MoOx. Adv. Sci. *7*, 2002395.

71. Kiermasch, D., Rieder, P., Tvingstedt, K., Baumann, A., and Dyakonov, V. (2016). Improved charge carrier lifetime in planar perovskite solar cells by bromine doping. Sci. Rep. *6*, 39333.

72. Mozer, A.J., Dennler, G., Sariciftci, N.S., Westerling, M., Pivrikas, A., Österbacka, R., and Juška, G. (2005). Time-dependent mobility and recombination of the photoinduced charge carriers in conjugated polymer/fullerene bulk heterojunction solar cells. Phys. Rev. B *72*, 1–10.

73. Neukom, M., Züfle, S., Jenatsch, S., and Ruhstaller, B. (2018). Opto-electronic characterization of third-generation solar cells. Sci. Technol. Adv. Mater. *19*, 291–316.

74. Dahlström, S., Liu, X., Yan, Y., Sandberg, O.J., Nyman, M., Liang, Z., and Österbacka, R. (2020). Extraction current transients for selective charge-carrier mobility determination in non-fullerene and ternary bulk heterojunction organic solar cells. ACS Appl. Energy Mater. *3*, 9190–9197.

75. Chen, Y., Peng, J., Su, D., Chen, X., and Liang, Z. (2015). Efficient and balanced charge transport revealed in planar perovskite solar cells. ACS Appl. Mater. Interfaces *7*, 4471–4475.

76. Ginting, R.T., Jung, E.S., Jeon, M.K., Jin, W . Y., Song, M., and Kang, J.W. (2016). Low-temperature operation of perovskite solar cells: with efficiency improvement and hysteresis-less. Nano Energy *27*, 569–576.

77. Aukštuolis, A., Girtan, M., Mousdis, G.A., Mallet, R., Socol, M., Rasheed, M., and Stanculescu, A. (2017). Measurement of charge carrier mobility in perovskite nanowire films by photo-celiv method. Proc. Rom. Acad. A *18*, 34–41.

78. Ritzer, D.B., Abzieher, T., Basibüyük, A., Feeney, T., Laufer, F., Ternes, S., Richards, B.S., Bergfeld, S., and Paetzold, U.W. (2022). Upscaling of perovskite solar modules: the synergy of fully evaporated layer fabrication and all-laser-scribed interconnections. Prog. Photovolt. Res. Appl. *30*, 360–373.

79. Zhu, J., Qian, Y., Li, Z., Gong, O.Y., An, Z., Liu, Q., Choi, J.H., Guo, H., Yoo, P.J., Kim, D.H., et al. (2022). Defect healing in FAPb(I1-xBrx)3 perovskites: multifunctional fluorinated sulfonate surfactant anchoring enables >21% modules with improved operation stability. Adv. Energy Mater. *12*, 1–12.